

***a* – *b* Anisotropy of the Intra-Unit-Cell Magnetic Order in  $\text{YBa}_2\text{Cu}_3\text{O}_{6.6}$** Lucile Mangin-Thro,<sup>1,\*</sup> Yuan Li,<sup>2,†</sup> Yvan Sidis,<sup>1</sup> and Philippe Bourges<sup>1</sup><sup>1</sup>Laboratoire Léon Brillouin, CEA-CNRS, Université Paris-Saclay, CEA Saclay, 91191 Gif-sur-Yvette, France<sup>2</sup>Max Planck Institute for Solid State Research, 70569 Stuttgart, Germany

(Received 18 October 2016; published 2 March 2017)

Within the complex phase diagram of the hole-doped cuprates, seizing the nature of the mysterious pseudogap phase is essential for unraveling the microscopic origin of high-temperature superconductivity. Below the pseudogap temperature  $T^*$ , evidence for intra-unit-cell orders breaking the fourfold rotation symmetry have been provided by neutron diffraction and scanning tunneling spectroscopy. Using polarized neutron diffraction on a detwinned  $\text{YBa}_2\text{Cu}_3\text{O}_{6.6}$  sample, we here report a distinct *a* – *b* anisotropy of the intra-unit-cell magnetic structure factor below  $T^*$ , highlighting that intra-unit-cell order in this material breaks the mirror symmetry of the  $\text{CuO}_2$  bilayers. This is likely to originate from a crisscrossed arrangement of loop currents within the  $\text{CuO}_2$  bilayer, resulting in a bilayer mean toroidal axis along the **b** direction.

DOI: 10.1103/PhysRevLett.118.097003

Upon doping with charge carriers, the lamellar copper oxides evolve from antiferromagnetic Mott insulators to high-temperature superconductors. On the underdoped side of their phase diagram [Fig. 1(a)], hole-doped cuprates exhibit unusual electronic and magnetic properties in the so-called pseudogap (PG) phase below  $T^*$  [1]. Among cuprate families, various studies in  $\text{YBa}_2\text{Cu}_3\text{O}_{6+x}$  (YBCO) have enabled researchers to obtain a particularly deep understanding of the PG phase. This bilayer system, the structure of which is shown in Fig. 1(b), becomes weakly orthorhombic owing to the formation of  $\text{CuO}$  chains upon increasing oxygen stoichiometry from  $x = 0$  to 1, but the  $\text{CuO}_2$  layers are commonly believed to retain a nearly tetragonal structure that leaves room for spontaneous breaking of the  $C_4$  rotational symmetry (into  $C_2$ ) in the electronic and/or magnetic structure. As a strain field, the weak orthorhombicity can facilitate observation of such symmetry breaking by eliminating one of the two possible domains, yielding an *a* – *b* anisotropy of physical properties that is much more pronounced than the structural orthorhombicity itself. Such an anisotropy has been reported in electrical transport [2], spin dynamics [3–5], the Nernst coefficient [6,7], and nuclear magnetic resonance [8] measured on detwinned single crystals. In the PG state of another bilayer cuprate  $\text{Bi}_2\text{Sr}_2\text{CaCu}_2\text{O}_{8+\delta}$  [9], scanning tunneling microscopy also highlighted an intra-unit-cell (IUC) electronic nematic state with unbalanced electronic density on oxygen sites along **a** and **b**.

The breaking of time reversal symmetry (TRS) is another feature of PG physics. Indeed, an IUC magnetic order develops below a temperature  $T_{\text{mag}}$ , matching  $T^*$ , as reported by polarized neutron diffraction in four cuprate families [10–18]. In YBCO, this order is long ranged at low doping [11,14], becomes short-ranged around optimal doping [19], and vanishes at high doping. This IUC

magnetic order indicates that translation invariance is preserved, but TRS is broken in the PG state. In addition, resonant ultrasound measurements reported a weak anomaly at  $T^*$ , indicating that the PG phase is a true broken symmetry state [20]. Recently, optical second-harmonic generation

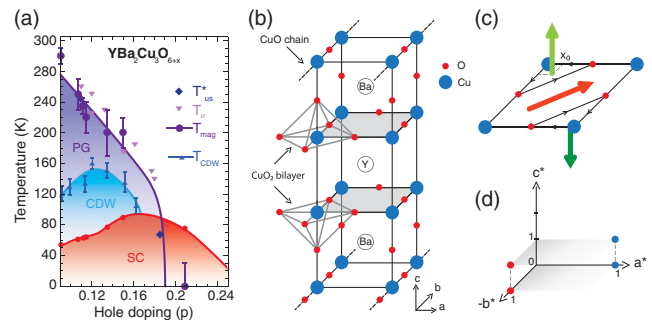


FIG. 1.  $\text{YBa}_2\text{Cu}_3\text{O}_{6+x}$  phase diagram and structure, and the loop currents as a possible model for the cuprates. (a)  $\text{YBa}_2\text{Cu}_3\text{O}_{6+x}$  phase diagram as a function of hole doping ( $p$ ), showing the PG, the incipient charge density wave (CDW) and superconducting (SC) phases. The following values are reported:  $T_{\text{us}}^*$  from resonant ultrasound measurements [20],  $T_{\text{mag}}$ , the temperature of the magnetic IUC order [16,19],  $T_{\nu}$ , the onset of *a* – *b* anisotropy from the Nernst effect [6], and  $T_{\text{CDW}}$ , the onset of CDW correlations from resonant x-ray measurements [34]. (b) Crystal structure of the bilayer compound  $\text{YBa}_2\text{Cu}_3\text{O}_{6+x}$  with the  $\text{CuO}$  chains running along **b**. (c) Loop current model [25,26]: each loop induces an orbital magnetic moment  $\mathbf{M}_i$  (green arrows) perpendicular to the  $\text{CuO}_2$  plaquette, located at the triangle center,  $x_0 = 0.146$ . The red arrow represents the associated anapole or toroidal moment  $\mathbf{T} \approx \sum_i \mathbf{M}_i \times \mathbf{r}_i$  ( $\mathbf{r}_i$  stands for the vector connecting the center of the unit cell and the location of the  $i$ th moment). (d) Location of the studied magnetic Bragg reflections: wave vectors, given in reduced lattice units, of the form of  $\mathbf{Q} = (1, 0, L)$  (blue circles) and  $\mathbf{Q} = (0, 1, L)$  (red circles) have been studied.

measurements in YBCO have further reported a global broken inversion symmetry at  $T^*$  [21], confirming that the pseudogap region coincides with a hidden order. Among other theoretical proposals [22–24], the most consistent interpretation of the IUC magnetism [19] remains the loop current (LC) model for the PG state [25–27]. It is found to coexist with electronic nematic order [28] as well as charge-density wave states [29,30]. The most promising type of LC pattern consists of two counterpropagating LCs flowing over copper and neighboring oxygen sites within each  $\text{CuO}_2$  unit cell, producing a pair of out-of-plane staggered orbital magnetic moments ( $\mathbf{M}_i = \pm \mathbf{M}$ ) separated along a given diagonal [Fig. 1(c)]. For a single  $\text{CuO}_2$  layer, four degenerate LC patterns exist, identified by their toroidal moment or anapole [26]  $\mathbf{T} = \sum_i \mathbf{r}_i \times \mathbf{M}_i$  [red arrow in Fig. 1(c)] along the other diagonal, along which the inversion symmetry is also broken. The associated IUC magnetic structure factor probed by neutron diffraction can, therefore, be anisotropic along both diagonals, but no  $a - b$  anisotropy is expected as far as a single  $\text{CuO}_2$  layer is concerned.

Motivated by the fact that in underdoped YBCO for a hole doping larger than  $p \sim 0.1$ , both the  $a - b$  anisotropy in the Nernst coefficient [6] and the IUC magnetic order are set below  $T^*$  [Fig. 1(a)], we have carried out a polarized neutron diffraction in a detwinned YBCO sample. We observe an  $a - b$  anisotropy in the IUC magnetic structure factor with distinct magnetic intensities along  $\mathbf{a}^*$  and  $\mathbf{b}^*$  which show that the mirror symmetry of the  $\text{CuO}_2$  bilayers is broken below  $T^*$ . Our data can be described by a crisscrossed arrangement of loop currents within the  $\text{CuO}_2$  bilayer, with a resulting toroidal axis along the  $\text{CuO}$  chain,  $\mathbf{b}$ , direction.

We here report polarized neutron measurements on a low-doped  $\text{YBa}_2\text{Cu}_3\text{O}_{6.6}$  ( $T_c = 63\text{K}$ ,  $p = 0.12$ ) detwinned single crystal, previously used to study spin dynamics [3]. The polarized neutron experiments have been performed on the triple-axis spectrometer 4F1 (Orphée, CEA-Saclay). A polarizing supermirror (bender) and a Mezei flipper are inserted on the incoming neutron beam in order to select neutrons with a given spin. In addition, a filter (pyrolytic graphite) is put before the bender to remove high harmonics. After the sample, the final polarization,  $\mathbf{P}$ , is analyzed by a Heusler analyzer. The incident and final neutron wave vector are set to  $k_I = k_F = 2.57 \text{ \AA}^{-1}$ . Following previous studies [10–19], the search for magnetic order in the pseudogap phase is performed on Bragg reflections  $\mathbf{Q} = (1, 0, L)/(0, 1, L)$  with integer  $L = 0, 1$  values. The general methods to extract the IUC magnetic signal have been discussed in Refs. [10–19], and the important steps for our analysis are reported in the Supplemental Material [31].

In order to compare the magnetic signals along the directions  $\mathbf{a}^* = [1, 0]$  [blue symbols in Fig. 1(d)] and  $\mathbf{b}^* = [0, 1]$  (red symbols), measurements were carried out at Bragg reflections of the form of  $\mathbf{Q} = (1, 0, L)/(0, 1, L)$  with  $L = 0$  or  $L = 1$  in reciprocal lattice units. Here, we

focus on the scattered magnetic intensity for two neutron spin polarizations  $\mathbf{P}$  (see the Supplemental Material [31]): (i)  $\mathbf{P} \parallel \mathbf{Q}$ , which measures the full magnetic scattering intensity and (ii)  $\mathbf{P} \perp \mathbf{Q}$  in the scattering plane, where predominantly the out-of-plane magnetic component,  $\mathbf{M}_c$ , is probed.

Figure 2 shows the raw neutron intensity on two Bragg peaks along the directions  $\mathbf{a}^*$  and  $\mathbf{b}^*$  for  $L = 0$  and  $\mathbf{P} \parallel \mathbf{Q}$ . The intensities for two neutron spin states are shown in the spin-flip (SF) channel, when the scattering process flips the neutron spin at the sample position, and the non-spin-flip (NSF) channel, when it is preserved. Following a standard procedure [10–12,14–16,19], both curves have been normalized at high temperature over some temperature range (here between 250 and 330 K). On the one hand, NSF intensity represents the nuclear Bragg peak intensity which exhibits a continuous decay when increasing the temperature as expected for a Debye-Waller factor. As the sample is detwinned, the NSF intensity along  $\mathbf{b}^*$  [Fig. 2(b)] is weaker than along  $\mathbf{a}^*$  [Fig. 2(a)]. On the other hand, the SF scattering intensity probes a true SF magnetic scattering (if any) on top of a polarization leakage of the NSF channel into the SF channel. The latter is given by the NSF intensity divided by the flipping ratio  $\text{FR}^0$ . For a perfectly spin-polarized neutron beam,  $\text{FR}^0$  goes to infinity and the leakage vanishes. On top of the normalized nuclear scattering, the SF intensity then exhibits an extra scattering at low temperature that is attributed to the IUC magnetic component (Fig. 2). In both the  $\mathbf{a}^*$  and  $\mathbf{b}^*$  directions, the magnetic signal appears below  $T_{\text{mag}} \sim 240$  K, in agreement with  $T_{\text{mag}} = 220 \text{ K} \pm 20 \text{ K}$  determined in an early study on the same sample matching  $T^* \sim 230 \text{ K}$  deduced from

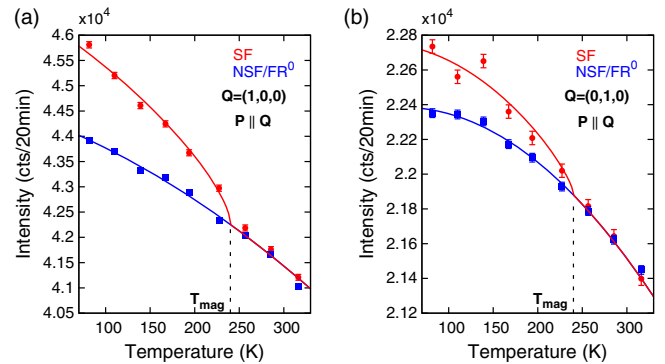


FIG. 2. Raw Bragg peaks intensity. Temperature dependence of the spin-flip (SF) (red circles) and non-spin-flip (NSF) (blue squares) neutron intensity for a neutron polarization  $\mathbf{P} \parallel \mathbf{Q}$ . (a) At  $\mathbf{Q} = (1, 0, 0)$  (along  $\mathbf{a}^*$ ). (b) At  $\mathbf{Q} = (0, 1, 0)$  (along  $\mathbf{b}^*$ ). In the SF channel, a magnetic signal is observed below  $T_{\text{mag}} \sim 240$  K on top of the NSF intensity normalized at high temperature by a constant flipping ratio,  $\text{FR}^0 \sim 40$ . Data have been averaged over a temperature range of 25 K to improve the statistics. Error bars of standard deviation are about the size of the points.

resistivity measurement at that doping [10]. Qualitatively, the magnetic signal for  $\mathbf{Q} = (0, 1, 0)$  is much weaker than for  $\mathbf{Q} = (1, 0, 0)$ , which underlines an  $a - b$  anisotropy of the  $Q = 0$  IUC magnetic signal.

To perform a more quantitative analysis of the magnetic scattering, we need to calibrate the change of neutron polarization with temperature. We performed a systematic analysis based on a generic procedure improved in previous studies [16,19]. We then determined the IUC magnetic intensity, which we report in Fig. 3, at four different Bragg spots for two different neutron polarization states. Figure 3(a) shows the full magnetic intensity for  $\mathbf{P} \parallel \mathbf{Q}$  at  $L = 0$  as a function of temperature. Quite remarkably, the full magnetic intensity exhibits a net difference between the two directions, being  $\sim 3$  times larger at  $\mathbf{Q} = (1, 0, 0)$  than at  $(0, 1, 0)$ . Increasing  $L$  to 1, Fig. 3(b), the magnetic intensity becomes almost identical in both directions, with slightly more intensity for  $(0, 1, 1)$ . A net  $a - b$  anisotropy of the IUC magnetic intensity thus exists, but, remarkably, changes as a function of  $L$ .

Rotating  $\mathbf{P} \perp \mathbf{Q}$  in the scattering plane, one selectively probes the scattering intensity  $\propto \mathbf{M}_c^2$ , which corresponds to the out-of-plane components of the magnetic moments. In Fig. 3(c), the magnetic intensity is at least 6 times larger at  $\mathbf{Q} = (1, 0, 0)$  than at  $(0, 1, 0)$ , where the magnetic intensity vanishes within error bars. At  $L = 1$  [Fig. 3(d)], the  $a - b$  anisotropy is fully reversed. Therefore, the anisotropy is more pronounced for the polarization  $\mathbf{P} \perp \mathbf{Q}$  than for the polarization  $\mathbf{P} \parallel \mathbf{Q}$ . Clearly, the out-of-plane components of

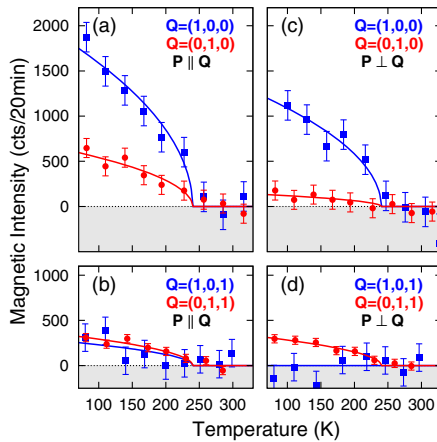


FIG. 3. Temperature dependence of the IUC magnetic intensity in both directions,  $\mathbf{a}^*$  (blue squares) and  $\mathbf{b}^*$  (red circles). Left panels show the polarization  $\mathbf{P} \parallel \mathbf{Q}$ , (a) at  $L = 0$  and (b) at  $L = 1$ . Right panels show the polarization  $\mathbf{P} \perp \mathbf{Q}$ , (c) at  $L = 0$  and (d)  $L = 1$ . Magnetic intensities are obtained using the procedure described in the Supplemental Material [31]. Each curve is described by the function  $I_0(1 - T/T_{\text{mag}})^{2\beta}$ , where  $I_0$  is fitted with  $\beta = 0.25$  and  $T_{\text{mag}} = 240$  K being fixed. Below this temperature, the amplitude of the magnetic intensity  $I_{\text{mag}}$  differs as a function of wave vector and polarization. Error bars are of standard deviation.

the magnetic moments are mainly responsible for the observed  $a - b$  anisotropy varying with  $L$ . (Results on the in-plane moment, which exhibits less anisotropy, will be presented elsewhere.)

Our study puts stringent constraints on the possible nature of the IUC magnetic order: (i) the magnetic structure factor has to be maximum at  $L = 0$  and (ii) the IUC order must produce a scattering pattern characterized by a remarkable  $a - b$  anisotropy varying with  $L$ , as revealed by a close comparison of magnetic intensities at  $(1, 0, L)$  and  $(0, 1, L)$ . The change of the structure factor along  $\mathbf{c}^*$ —odd in  $L$  along  $\mathbf{a}^*$  and even in  $L$  along  $\mathbf{b}^*$ —suggests that the bilayer structure of IUC order does not represent the symmetries of the higher-temperature phase, i.e., that the symmetry is truly broken. More specifically, it indicates that the bilayer mirror plane across the Y site is broken in the pseudogap phase of YBCO. In particular, the mentioned above requirements cannot be fulfilled by magnetic nematic states, which involve spin or orbital moments located on oxygen sites [10,22]. Indeed, these magnetic patterns fail to reproduce a  $L$ -dependent  $a - b$  anisotropy for the out-of-plane magnetic scattering intensity. This is at variance with a crisscrossed arrangement of loop currents that we describe below.

The LC model naturally induces staggered out-of-plane magnetic moments. For a single  $\text{CuO}_2$  layer, as discussed above, there are four LC degenerate patterns, none of which is expected to give rise to the observed  $a - b$  anisotropy. However, in a bilayer system such as YBCO, one needs to consider the relative arrangement of LC patterns in the two  $\text{CuO}_2$  layers, labeled (1) and (2), separated along the  $\mathbf{c}$  axis by a distance  $d = 0.28c$ . This yields  $4 \times 4$  possible magnetic configurations, which can be classified into four distinct groups of LC patterns (Fig. 4) and identified by the resulting toroidal axis  $(\mathbf{T}_1 + \mathbf{T}_2)$ . Each group breaks

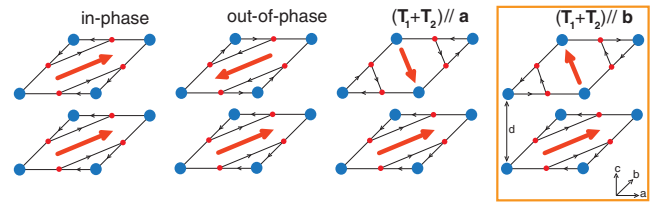


FIG. 4. Possible model for the  $a - b$  anisotropy of the IUC magnetic intensity. Choosing one possible loop-current state over the four existing ones for the lower plane (1) and varying the state for the upper plane (2), one obtains four different types of configurations: in-phase, out-of-phase anapoles, and two situations where the sum of anapoles in both planes gives a resultant either along  $\mathbf{a}$  or  $\mathbf{b}$ . The last one is selected by the experimental results. Each of these configurations is 4 times degenerate, as one could select a different LC state for the lower plane. However, the upper plane configuration would always be correlated with the first plane as discussed here. The LC structure factor depends only on the relative configurations of both planes (see the Supplemental Material [31]).

different symmetries: in the first two groups, the different configurations are connected by  $C_4$  rotation, whereas in the last two groups the configurations are connected by  $C_2$  rotation (equivalent to time reversal) and breaks the bilayer mirror symmetry. Each group is characterized by a specific magnetic structure factor shown in Table I.

If within the bilayer LC patterns are either in phase or out of phase (where  $\mathbf{T}_1$  and  $\mathbf{T}_2$  are parallel or antiparallel), the scattered magnetic intensity is respectively modulated by  $|2 \cos[\pi(d/c)L]|^2$  or  $|2 \sin[\pi(d/c)L]|^2$  along both  $\mathbf{a}^*$  or  $\mathbf{b}^*$ . The in-phase configuration has been previously favored [10,14–16,19] since the IUC intensity is the strongest at Bragg peaks with  $L = 0$  (which actually dismisses the out-of-phase case). However, we here observe that the IUC intensity varies with  $L$  differently along the directions  $\mathbf{a}^*$  and  $\mathbf{b}^*$ . Both of these configuration groups are thus inconsistent with our observations.

The two other configuration groups are featured by a crisscrossed arrangement of LC patterns, and are further identified owing to the orientation of their resulting toroidal axis ( $\mathbf{T}_1 + \mathbf{T}_2$ ) parallel to either  $\mathbf{a}$  or  $\mathbf{b}$ . These two configurations break the mirror symmetry at the middle of the bilayers (the Y site) as requested by the experiment. Importantly, the energy difference between these two groups is expected to be linearly coupled to the orthorhombicity. Therefore, any orthorhombic distortion would remove the degeneracy between both configurations. Interestingly, they exhibit out-of-phase modulations of the scattering intensities at  $(1, 0, L)$  and  $(0, 1, L)$ , yielding an  $L$ -dependent  $a - b$  anisotropy of the scattering intensity (Table I). Only the configuration  $(\mathbf{T}_1 + \mathbf{T}_2) \parallel \mathbf{b}$  gives rise to a magnetic intensity larger for  $(1, 0, 0)$  than  $(0, 1, 0)$ . Using the structure factor of Table I, one remarks that the anisotropy weakens and is even reversed at  $L = 1$ . This evolution of the magnetic intensities is consistent with the experimental observations (Fig. 3). Nevertheless, a weaker or even null intensity for  $(1, 0, 1)$  is observed [Fig. 3(c)]. That could simply be due to limited statistics or, more interestingly, could be related by a larger distance  $d/c$  separating the moments. Note that, in models that include the apical oxygens [12,32], the LCs could be delocalized and a larger distance  $d/c$  would occur and can further reduce intensity at  $(1, 0, 1)$  than at  $(0, 1, 1)$ . Globally, the LC configuration in Fig. 4 with  $(\mathbf{T}_1 + \mathbf{T}_2) \parallel \mathbf{b}$  accounts for the polarized neutron data. This particular arrangement of LC within the bilayer is a truncated version of the

chiral LC order considered by Pershoguba *et al.* [33] as a pattern of a cholesteric arrangement of toroidal moments. In contrast to our results, the proposed full chiral LC order [33] would double the magnetic unit cell along  $\mathbf{c}$  and shift the magnetic Bragg reflection at half-integer  $L$  values. This is not what is happening; instead, we here demonstrate that the direction of the resulting toroidal axis ( $\mathbf{T}_1 + \mathbf{T}_2$ ) is always pinned down along  $\mathbf{b}$ , i.e., the CuO chain direction.

On general grounds, it is interesting to relate our finding to the electronic nematicity, which has been abundantly discussed in the context of cuprates [2–8] even occurring within the unit cell [9]. Our study shows that the resulting toroidal moment for a bilayer presents an Ising anisotropy along the CuO chain. By itself, the presence of an  $a - b$  anisotropy that pins the direction of a vector magnetic order parameter does not amount to nematicity; this is because nematic order is characterized by a director, and not a vector order parameter, such as the anapoles of Fig. 4. However, we show that the magnetic structure of the IUC order reveals an unexpected  $a - b$  anisotropy due to the bilayer structure of YBCO and its weak orthorhombic distortion. Therefore, our study suggests that there could exist an interplay between a crisscrossed LC order and the reported nematicity in YBCO [2,3,6,7], an intriguing scenario that has not so far been considered. One can further notice the good agreement of the nematicity deduced from the Nernst effect with the onset of the IUC order [Fig. 1(a)] that explicitly occur at temperatures higher than the CDW signal [34]. Using a single-band model to discuss the instabilities of a weakly correlated Fermi liquid [35], the nematicity appears as a spontaneous distortion of the Fermi surface ( $d$ -wave Pomeranchuk instability). Within the three-band Emery model, it has been shown that intra-unit-cell instabilities such as LC order and electronic nematicity could coexist [28]. It might be interesting to reexamine the role of the bilayer in light of our results.

Finally, the charge order that develops well below  $T^*$  in YBCO also exhibits an  $a - b$  anisotropy [8] with a remarkable  $L$ -dependent  $a - b$  anisotropy of its superstructure reflections in hard x-ray diffraction measurements [36]. The analysis and modeling of x-ray diffraction measurements [36] indicate as well that the reported quasi-2D CDW breaks the mirror symmetry of the CuO<sub>2</sub> bilayers in YBCO, as does the crisscrossed LC states that

TABLE I.  $L$  dependence of the out-of-plane magnetic structure factor for each group of LC magnetic patterns (different bilayer correlation) of Fig. 4 at  $\mathbf{Q} = (1, 0, L)$  and  $\mathbf{Q} = (0, 1, L)$  (see the structure factor calculation in the Supplemental Material [31]).

LCs	In phase	Out of phase	$(\mathbf{T}_1 + \mathbf{T}_2) \parallel \mathbf{a}$	$(\mathbf{T}_1 + \mathbf{T}_2) \parallel \mathbf{b}$
$(1, 0, L)$	$\propto \cos^2[\pi(d/c)L]$	$\propto \sin^2[\pi(d/c)L]$	$\propto \sin^2[\pi(d/c)L]$	$\propto \cos^2[\pi(d/c)L]$
$(0, 1, L)$	$\propto \cos^2[\pi(d/c)L]$	$\propto \sin^2[\pi(d/c)L]$	$\propto \cos^2[\pi(d/c)L]$	$\propto \sin^2[\pi(d/c)L]$

we are reporting here. This raises questions concerning a possible interplay between CDW and the crisscrossed LC states.

We thank Marc-Henri Julien, Bernhard Keimer, Arkady Shekhter, Chandra Varma, and Victor Yakovenko for valuable discussions. We also acknowledge financial support from grants of the Agence Nationale pour la Recherche (ANR): UNESCOS (Contract No. ANR-14-CE05-0007) and NirvAna (Contract No. ANR-14-OHRI-0010).

---

\*Present address: Institut Laue-Langevin, 71 avenue des martyrs, 38000 Grenoble, France.

†Present address: International Center for Quantum Materials, School of Physics, Peking University, Beijing 100871, China.

- [1] B. Keimer, S. A. Kivelson, M. R. Norman, S. Uchida, and J. Zaanen, *Nature (London)* **518**, 179 (2016).
- [2] Y. Ando, K. Segawa, S. Komiyama, and A. N. Lavrov, *Phys. Rev. Lett.* **88**, 137005 (2002).
- [3] V. Hinkov, P. Bourges, S. Pailhès, Y. Sidis, A. Ivanov, C. D. Frost, T. G. Perring, C. T. Lin, D. P. Chen, and B. Keimer, *Nat. Phys.* **3**, 780 (2007).
- [4] V. Hinkov, D. Haug, B. Fauque, P. Bourges, Y. Sidis, A. Ivanov, C. Bernhard, C. T. Lin, and B. Keimer, *Science* **319**, 597 (2008).
- [5] D. Haug, V. Hinkov, Y. Sidis, P. Bourges, N. B. Christensen, A. Ivanov, T. Keller, C. T. Lin, and B. Keimer, *New J. Phys.* **12**, 105006 (2010).
- [6] R. Daou *et al.*, *Nature (London)* **463**, 519 (2010).
- [7] O. Cyr-Choinière, G. Grissonnanche, S. Badoux, J. Day, D. A. Bonn, W. N. Hardy, R. Liang, N. Doiron-Leyraud, and L. Taillefer, *Phys. Rev. B* **92**, 224502 (2015).
- [8] T. Wu, H. Mayaffre, S. Krämer, M. Horvatić, C. Berthier, W. N. Hardy, R. Liang, D. A. Bonn, and M.-H. Julien, *Nat. Commun.* **6**, 6438 (2015).
- [9] M. J. Lawler *et al.*, *Nature (London)* **466**, 347 (2010).
- [10] B. Fauqué, Y. Sidis, V. Hinkov, S. Pailhès, C. T. Lin, X. Chaud, and P. Bourges, *Phys. Rev. Lett.* **96**, 197001 (2006).
- [11] H. A. Mook, Y. Sidis, B. Fauqué, V. Balédent, and P. Bourges, *Phys. Rev. B* **78**, 020506 (2008).
- [12] Y. Li, V. Balédent, N. Barišić, Y. Cho, B. Fauqué, Y. Sidis, G. Yu, X. Zhao, P. Bourges, and M. Greven, *Nature (London)* **455**, 372 (2008).
- [13] Y. Li, V. Balédent, N. Barišić, Y. C. Cho, Y. Sidis, G. Yu, X. Zhao, P. Bourges, and M. Greven, *Phys. Rev. B* **84**, 224508 (2011).
- [14] P. Bourges and Y. Sidis, *C. R. Physique* **12**, 461 (2011).
- [15] Y. Sidis and P. Bourges, *J. Phys. Conf. Ser.* **449**, 012012 (2013).
- [16] V. Balédent, D. Haug, Y. Sidis, V. Hinkov, C. T. Lin, and P. Bourges, *Phys. Rev. B* **83**, 104504 (2011).
- [17] S. De Almeida-Didry, Y. Sidis, V. Balédent, F. Giovannelli, I. Monot-Laffez, and P. Bourges, *Phys. Rev. B* **86**, 020504 (2012).
- [18] L. Mangin-Thro, Y. Sidis, P. Bourges, S. De Almeida-Didry, F. Giovannelli, and I. Laffez-Monot, *Phys. Rev. B* **89**, 094523 (2014).
- [19] L. Mangin-Thro, Y. Sidis, A. Wildes, and P. Bourges, *Nat. Commun.* **6**, 7705 (2015).
- [20] A. Shekhter, B. J. Ramshaw, R. Liang, W. N. Hardy, D. A. Bonn, F. F. Balakirev, R. D. McDonald, J. B. Betts, S. C. Riggs, and A. Migliori, *Nature (London)* **498**, 75 (2013).
- [21] L. Zhao, C. A. Belvin, R. Liang, D. A. Bonn, W. N. Hardy, N. P. Armitage, and D. Hsieh, *Nat. Phys.* (2016).
- [22] A. S. Moskvina, *JETP Lett.* **96**, 385 (2012).
- [23] S. W. Lovesey, D. D. Khalyavin, and U. Staub, *J. Phys. Condens. Matter* **27**, 292201 (2015).
- [24] M. Fiehn, M. J. A. Fierz, F. Thöle, U. Staub, and N. A. Spaldin, *Phys. Rev. B* **93**, 174419 (2016).
- [25] C. M. Varma, *Phys. Rev. B* **73**, 155113 (2006).
- [26] A. Shekhter and C. M. Varma, *Phys. Rev. B* **80**, 214501 (2009).
- [27] Y. He and C. M. Varma, *Phys. Rev. B* **86**, 035124 (2012).
- [28] M. H. Fischer and E.-A. Kim, *Phys. Rev. B* **84**, 144502 (2011).
- [29] D. F. Agterberg, D. S. Melchert, and M. K. Kashyap, *Phys. Rev. B* **91**, 054502 (2015).
- [30] V. S. deCarvalho, C. Pépin, and H. Freire, *Phys. Rev. B* **93**, 115144 (2016).
- [31] See Supplemental Material at <http://link.aps.org/supplemental/10.1103/PhysRevLett.118.097003> for experimental details, the analysis of experimental results and the neutron structure factor calculation for loop currents in a bilayer.
- [32] C. Weber, A. Läuchli, F. Mila, and T. Giamarchi, *Phys. Rev. Lett.* **102**, 017005 (2009).
- [33] S. S. Pershoguba, K. Kechedzhi, and V. M. Yakovenko, *Phys. Rev. Lett.* **111**, 047005 (2013).
- [34] S. Blanco-Canosa, A. Frano, E. Schierle, J. Porras, T. Loew, M. Minola, M. Bluschke, E. Weschke, B. Keimer, and M. Le Tacon, *Phys. Rev. B* **90**, 054513 (2014).
- [35] V. S. Oganessian, S. A. Kivelson, and E. Fradkin, *Phys. Rev. B* **64**, 195109 (2001).
- [36] E. M. Forgan *et al.*, *Nat. Commun.* **6**, 10064 (2015).